ADVANCED MATERIALS INTERFACES
Open Access
www.advmatinterfaces.de

Atomistic Understanding of the Coherent Interface Between Lead Iodide Perovskite and Lead Iodide

Mathias Uller Rothmann, Kilian B. Lohmann, Juliane Borchert, Michael B. Johnston, Keith P. McKenna, Laura M. Herz, and Peter D. Nellist**

Metal halide perovskite semiconductors have shown great performance in solar cells, and including an excess of lead iodide (PbI_2) in the thin films, either as mesoscopic particles or embedded domains, often leads to improved solar cell performance. Atomic resolution scanning transmission electron microscope micrographs of formamidinium lead iodide ($FAPbI_3$) perovskite films reveal the $FAPbI_3$:PbI_2 interface to be remarkably coherent. It is demonstrated that such interface coherence is achieved by the PbI_2 deviating from its common 2H hexagonal phase to form a trigonal 3R polytype through minor shifts in the stacking of the weakly van-der-Waals-bonded layers containing the near-octahedral units. The exact crystallographic interfacial relationship and lattice misfit are revealed. It is further shown that this 3R polytype of PbI_2 has similar X-ray diffraction (XRD) peaks to that of the perovskite, making XRD-based quantification of the presence of PbI_2 unreliable. Density functional theory demonstrates that this interface does not introduce additional electronic states in the bandgap, making it electronically benign. These findings explain why a slight PbI_2 excess during perovskite film growth can help template perovskite crystal growth and passivate interfacial defects, improving solar cell performance.

1. Introduction

Lead halide perovskite semiconductors have made significant advances over the past decade as light-absorber layers in thin-film solar cells with power conversion efficiencies now reaching 26 %.[1] While lead halide perovskites have excellent optoelectronic properties, such as long charge-carrier mobilities and diffusion lengths,[2,3] much of their success derives from their benign defect chemistry. Given that lead halide perovskite absorber layers have generally been deposited through relatively simple solution-processing[4,5] or vapor-deposition[6,7] routes, their relative lack of electronic defects that trap charge carriers[8,9] has been remarkable. Initial analysis of the benign defect chemistry of lead halide perovskites has mostly focused on the formation dynamics of point defects, such as interstitials, vacancies, and substitutions, showing that those associated with relatively shallow energetic levels situated near band edges are most likely to form.[10,11] However, as the field has progressed, focus has increasingly shifted towards the nature of defects associated with interfaces formed either between perovskite grains, or with other materials, such as charge extraction layers or precursor remnants.[12,13]

In this context, knowledge of the interfaces introduced into the lead halide perovskites through the inclusion of precursor remnants is particularly important. Lead halide perovskite films are generally fabricated from a combination of both lead

M. U. Rothmann, K. B. Lohmann, J. Borchert, M. B. Johnston, L. M. Herz
Department of Physics
University of Oxford
Clarendon Laboratory, Parks Road, Oxford OX1 3PU, UK
E-mail: laura.herz@physics.ox.ac.uk

M. U. Rothmann
Foshan Xianhu Laboratory of the Advanced Energy Science and Technology Guangdong Laboratory
Xianhu Hydrogen Valley
Foshan 528200, P. R. China

The ORCID identification number(s) for the author(s) of this article can be found under https://doi.org/10.1002/admi.202300249

DOI: 10.1002/admi.202300249

K. P. McKenna
School of Physics, Engineering and Technology
University of York, Heslington
York YO10 5DD, UK

L. M. Herz
Institute for Advanced Study
Technical University of Munich
Lichtenbergstrasse 2a, D-85748 Garching, Germany

P. D. Nellist
Department of Materials
University of Oxford
16 Parks Road, Oxford OX1 3PH, UK
E-mail: peter.nellist@materials.ox.ac.uk

iodide (PbI_2) and organo-halide (e.g., formamidinium (FA) or methylammonium (MA) iodide) precursors,[4–6] opening the possibility of remnants being incorporated. Fortunately, experimental investigations have repeatedly suggested that the fabrication of lead halide perovskites with a PbI_2 excess compared to stoichiometric requirements need not be detrimental to photovoltaic performance, but can indeed lead to improved solar cell performance.[14–23] However, the reasons for the apparently benign, or even favorable, nature of the perovskite:PbI_2 interface are still not fully understood. It is generally thought that including a certain small excess amount of PbI_2 in the photoactive layer leads to higher overall solar cell performance through a combination of surface and grain boundary defect passivation,[14–17,19–21] and by improving the overall film morphology and grain size.[16,24] However, PbI_2 can also negatively influence the overall long-term stability of perovskite solar cells.[19,25] Mesoscopic PbI_2 grains are commonly found at grain boundaries and at interfaces, and are believed to decrease the defect density at the grain boundaries by preventing I_{Pb} anti-site defects and the under-coordination of Pb atoms.[26,27] While this effect has been shown repeatedly through macroscopic experiments, it does leave open questions regarding the atomic nature of the interface between the perovskite phase and the PbI_2.

The most commonly observed phase of PbI_2 is hexagonal 2H, as a result of which reflections from the 2H phase are generally used to identify the presence of PbI_2 by X-ray diffraction (XRD) in perovskite films.[28] The substantial difference in geometry between hexagonal PbI_2 and cubic/tetragonal lead halide perovskites used for photovoltaic applications means that these phases should not be able to interface coherently. As a result, such interfaces should exhibit a high density of defects rather than providing the observed passivating effects. Similarly, this geometric difference would prevent epitaxial growth of perovskite from a PbI_2 seed, limiting the ability of PbI_2 to act as a growth scaffold for perovskite and thus prevent PbI_2 from increasing the size of perovskite grains. Thus, the experimental observations of the relatively benign[20] effects of PbI_2 excess seem difficult to reconcile with the inclusion of 2H hexagonal PbI_2.

These considerations highlight the pressing need for a full understanding of the interface between lead halide perovskites and their PbI_2 inclusions at an atomistic level. Here, we demonstrate why such interfaces, despite their geometric dissimilarities, can interface coherently without the introduction of local defects and associated trap states. We had recently suggested that a distortion of the PbI_2 lattice can lead to coherency with the $FAPbI_3$ lattice.[12] In the present work, we show that the proposed distortion leads to a previously observed 3R trigonal form of PbI_2[29] that forms completely coherent interfaces with $FAPbI_3$. We analyze low-dose low angle annular dark field scanning transmission electron microscope (LAADF STEM) images to provide a full crystallography of the interfacial relationship with $FAPbI_3$. We argue that the presence of the 3R trigonal phases of PbI_2 in the perovskite are facilitated by the crystallographic makeup of PbI_2, which enables a wide range of polytypes.[30–32] Distortions away from the common 2H hexagonal phase are easily afforded by the geometric flexibility of PbI_2 owing to a combination of ionically bonded near-octahedral units forming sheets held together by weaker van der Waals forces, with more than 20 polytypes found in the Inorganic Structural Database.[32] We further show that the coherent interface formed between the 3R trigonal polytype of PbI_2 favored at the interface with $FAPbI_3$ is electronically benign. Density functional theory reveals that this interface does not introduce further states in the bandgap of either surrounding material or at the interface itself. Our analysis therefore explains why some PbI_2 inclusions in perovskite need not be detrimental to photovoltaic device performance.

2. Results and Discussion

The careful use of low-dose (scanning) transmission electron microscopy (STEM), and in particular low-angle annular dark field (LAADF) imaging, has enabled the study of the crystallographic properties of hybrid perovskite thin films with up to atomic resolution, enabling the direct observation of a range of defects.[12,33,34] **Figure 1** shows a LAADF image of a PbI_2 domain in cubic $FAPbI_3$ viewed along the ⟨100⟩ zone-axis. The pixel intensity distribution of a LAADF micrograph depends on the average atomic number of an atomic column, and can therefore be used to assess the relative compositions of an imaged material. Figure 1d shows the intensity profile across the red line in Figure 1a. From approximately 0 to 6 nm and from 18 to 26 nm, a characteristic perovskite intensity profile is observed, alternating between high and low intensity. This profile is caused by the difference in average atomic number in the Pb/I columns and the I-only columns, with the Pb/I columns generating a higher pixel intensity than the I-only (see Figure S1, Supporting Information for a model of the perovskite structure). Within the PbI_2 (approximately 6 to 18 nm), however, there is no such alternation between the columns, showing that each atomic column must contain the same average atomic number but with the average atomic number in each column lying between that of the Pb/I and I-only columns .

While several crystal domains are visible in the micrograph in Figure 1a, the Fourier transform (FT) in Figure 1b, obtained from all of Figure 1a, appears to contain only a single pattern, indexed with cubic $FAPbI_3$ indices denoted by the 'c' subscript. The slight deviation from a square pattern is due to sample drift during image recording. The singular pattern is strong evidence of the perovskite and PbI_2 crystals observed in Figure 1a interfacing coherently, which is not possible for the hexagonal 2H polytype. Isolating the FT from the PbI_2 inclusion, as shown in Figure 1c, illustrates the lack of the perovskite $\{100\}_c$ planes, further highlighting the differences in crystallography between the two phases. It is clear that the particular PbI_2 phase being observed must have plane spacings that correspond to that of the $\{200\}_c$ planes, while at the same time maintaining a geometry that enables the coherent interfacing.

PbI_2 is structurally a highly flexible material with many known polytypes.[30–32] A full description of the polytypism of PbI_2 is beyond the scope of this paper, but is discussed in more detail in reference.[32] The polytypism is straightforward to understand by looking at **Figure 2**a; PbI_2 consists of sheets of $[PbI_6]^{4-}$ near-octahedral units (light blue rhombus) with strong bonding between the composing iodide and lead ions (orange bonds). The sheets in turn are relatively weakly bonded to each other through van der Waals interactions (red bonds). While the bonding is strong between the lead and iodide ions within the near-octahedral units, the relatively weak van der Waals bonding

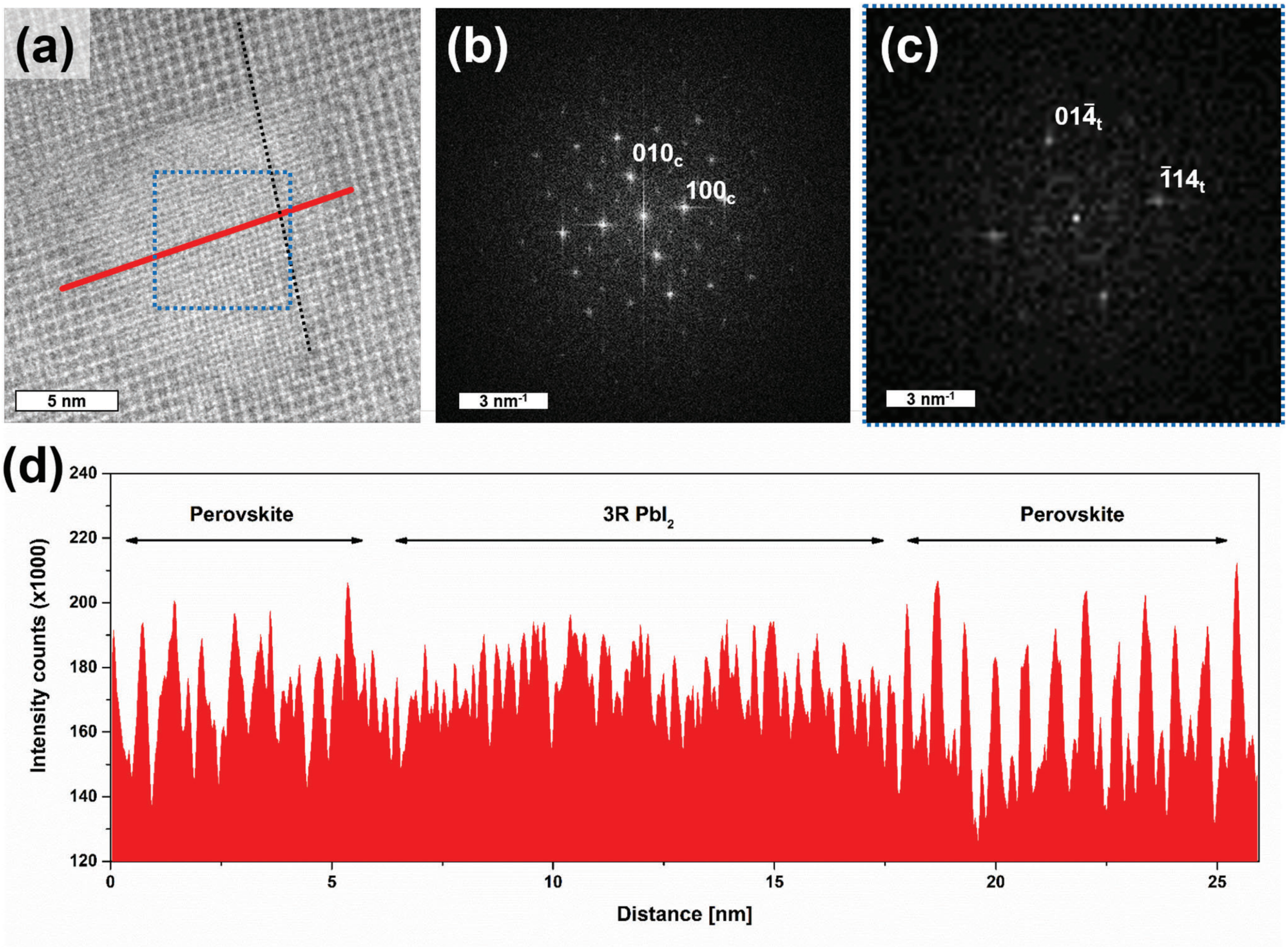

Figure 1. LAADF STEM micrograph and associated spatial frequencies of a PbI_2 domain in cubic $FAPbI_3$. a) Real-space micrograph showing a $FAPbI_3$ crystal with a coherent PbI_2 domain growing within the perovskite lattice. b) Fourier transform (FT) of (a) showing the near-pristine nature of the perovskite crystal. c) Fourier transform of the crystal in the dashed blue square in (a) showing the lack of the $\{100\}_c$ perovskite planes. d) Intensity profile along the red line crossing the PbI_2 inclusion in (a) showing the characteristic alternating high/low intensity of a perovskite crystal surrounding the uniform intensity frequency of PbI_2.

between the sheets enables a certain degree of shearing and changes in sheet spacing, and some small variation in bond angles within the near-octahedral units has also been observed.[32] Combining these two effects leads to a large number of polytypes.

The octahedral units within PbI_2 polytypes are very similar to those found in hybrid lead iodide perovskites and help explain the ease with which the two compounds can form from each other.[35] In the most common 2H polytype, the octahedral units do not align when viewed parallel to one of the Pb-I bonds in an octahedron. Figure 2b similarly shows how the geometry of the sheets and the near-octahedral units does not align with that of the cubic $FAPbI_3$, but it is clear that a shift of the sheets (illustrated in Figure S2, Supporting Information), to the form shown in **Figure 3**, would cause near-perfect alignment.

The $[PbI_6]^{4-}$ octahedra in the PbI_2 phase have bond lengths that match within 1% of the octahedra in the perovskite and because of the adjustable nature of the interlayer Van der Waals bonding, we have constructed a PbI_2 structure that is perfectly coherent with the $FAPbI_3$. We have identified this shifted polytype as being a trigonal 3R polytype (CIF card available in the Supporting Information). The polytype is able to interface coherently with cubic $FAPbI_3$ on the cubic (100), (010), and (001) planes. The crystallographic interfacial relationships are most clearly expressed using Miller-Bravais indices for the trigonal lattice. The three mutually perpendicular planes parallel to the cube planes are $(10\bar{1}4)$, $(\bar{1}104)$, and $(0\bar{1}14)$. The three mutually perpendicular directions that are parallel to the perovskite cube axes are $[40\bar{4}1]$ (which is equivalent to [841] in three-index notation), $[\bar{4}401]$ (equivalent to $[\bar{4}41]$) and $[0\bar{4}41]$ (equivalent to $[\bar{4}\bar{8}1]$). Because of the adjustable nature of the interlayer van der Waals bonding, we have assumed a PbI_2 structure that is perfectly coherent with the $FAPbI_3$. Experimentally we have never observed misfit defects at this interface in our STEM imaging studies. The atomic columns in the PbI_2 viewed along the $[40\bar{4}1]$ direction contain the sequence of atoms Pb-I-□-I (where □ indicates no atom occupying site), which have an average atomic number lying between that of the Pb-I-Pb-I and □-I-□-I columns of the

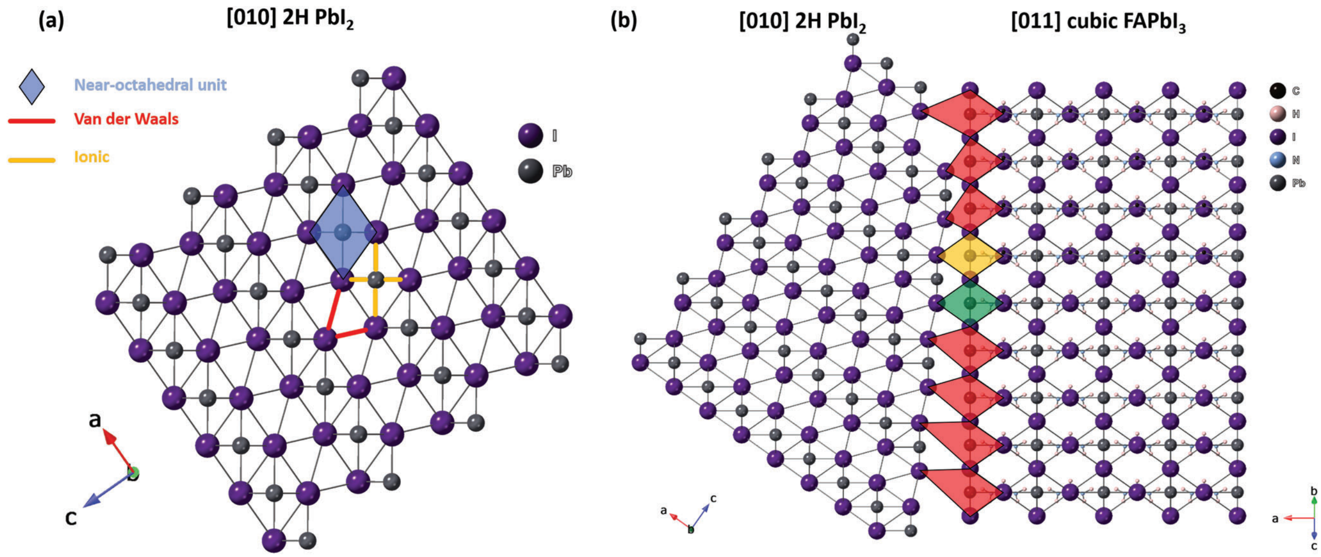

Figure 2. a) [010]-oriented 2H PbI_2 crystal model illustrating the sheets of ionically bonded (orange bonds) near-octahedral units (light blue shade). The sheets themselves are bonded through Van der Waals bonding (red bonds). In the 2H polytype, the I-Pb-I bonds within the near-octahedral units do not align with the I-I bonds between the sheets. b) Crystal model of the interface between a [010]-oriented 2H polytype of PbI_2 (left) and [011]-oriented cubic $FAPbI_3$ (right). The mismatch in geometry is illustrated by the distorted "octahedra" (red) that would appear around a coherently aligned octahedron (green). The yellow octahedron is only slightly distorted due to the slight difference in Pb-I-Pb bond lengths between the two phases.

perovskite, thereby explaining the column intensities seen in Figure 1 and further confirming our identification of the trigonal lattice. It is likely that the slight deformation needed to form the trigonal polytype with coherent interfaces with the perovskite is energetically favorable compared to forming defects at the interface between surrounding cubic perovskite and the PbI_2 domains. A similar trigonal polytype has previously been observed as a surface layer on 2D Ruddlesden-Popper perovskite,[29] but not as a coherently interfacing domain within a perovskite lattice.

As can be seen in Figure 3, because equivalent planes in the PbI_2 have half the spacing of equivalent planes in the perovskite, a shift of the cubic perovskite by half a unit cell lattice parameter generates an equivalent interface. We note that the pristine state of the surrounding perovskite lattice, and the shift of half a perovskite unit cell across the PbI_2 crystal along the dotted black line in Figure 1a, is strong evidence that the 3R PbI_2 observed here is not the result of beam damage but is remnant precursory material from which the perovskite growth has seeded. It is unlikely that growth of PbI_2 within the perovskite through irradiation damage would lead to such a half unit cell shift. Growth of perovskite on the PbI_2 can lead to a half unit-cell uncertainty in position, explaining the half unit cell shift of the perovskite

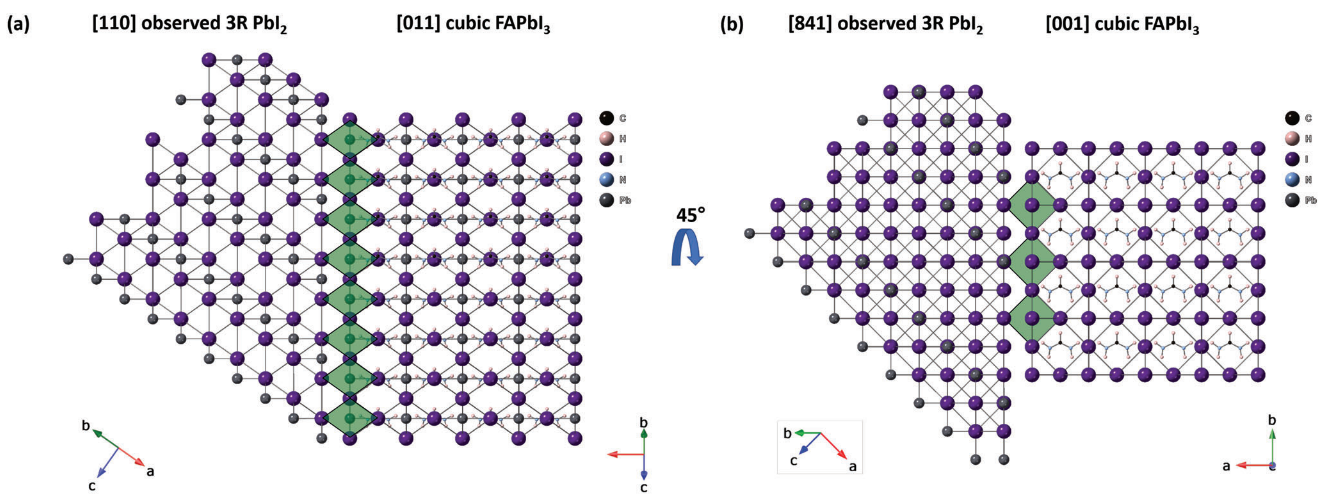

Figure 3. Crystal model of the interface between cubic $FAPbI_3$ and a trigonal 3R polytype of PbI_2 along the (100) plane of $FAPbI_3$, in which the bond distances and angles allow the crystals to interface coherently. a) shows the interface along the [011] $FAPbI_3$ axis and b) shows it along the [001] axis. The (104) plane and [110] direction in the trigonal PbI_2 are parallel to the (100) plane and [011] direction in cubic $FAPbI_3$, respectively.

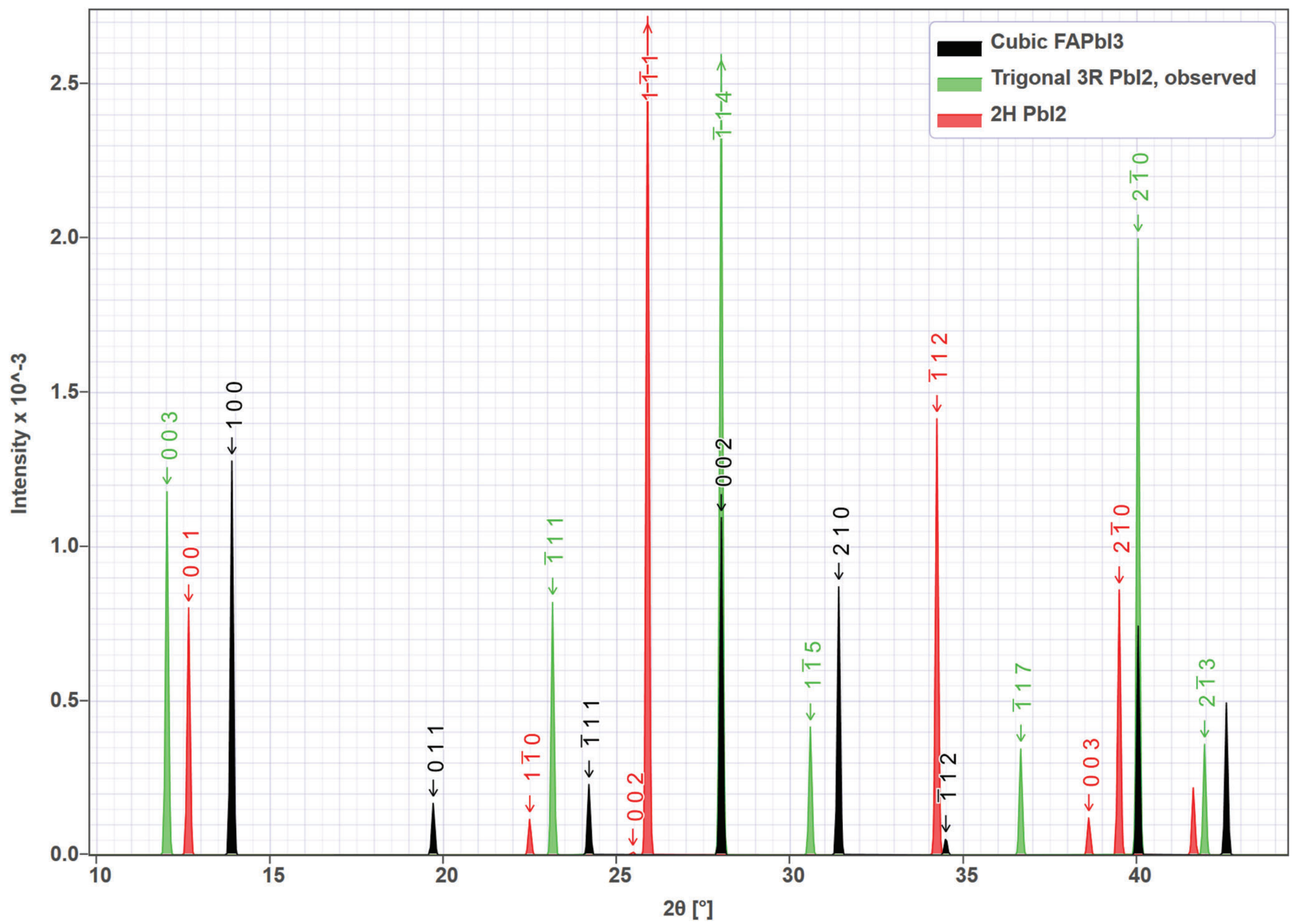

Figure 4. Simulated XRD patterns of the cubic phase of $FAPbI_3$ as well as various polytypes of PbI_2, simulated using Cu-Kα X-rays with a wavelength of 1.541 Å. The peaks around 26° and 35° are often used to identify the presence of PbI_2 are only unique to the 2H phase.

on either side of the PbI_2 particle. We have also found that while 3R PbI_2 is present intrinsically within cubic perovskite, it is also the first phase formed when $FAPbI_3$ is exposed to electron irradiation. Figure S3 (Supporting Information) shows the progression of a $FAPbI_3$ thin film as a function of electron dose. The pristine perovskite structure, shown in Figure S3a,d (Supporting Information), quickly changes under brief electron irradiation, as shown in Figure S3b,e (Supporting Information). The loss of the $\{100\}_c$ spots indicate a breakdown of the perovskite structure, but the square FT in Figure S3e ((Supporting Information) indicates that this phase is not hexagonal 2H PbI_2, but in fact the observed trigonal 3R phase. Hexagonal 2H PbI_2 forms after extended electron irradiation, as evidenced by the changes in geometry in Figure S3c (Supporting Information) and the additional spots in the orange circles in Figure S3f (Supporting Information).

The simulated selected area electron diffraction (SAED) patterns of $FAPbI_3$ and the observed 3R PbI_2 correspond very well to the Fourier transforms observed in Figure 1b. Figure S3g (Supporting Information) shows simulated electron diffraction patterns of [100]-oriented cubic $FAPbI_3$, [841]-oriented trigonal 3R PbI_2, and [101]-oriented hexagonal 2H PbI_2. It is clear that while certain diffraction spots overlap between $FAPbI_3$ (black spots) and 2H PbI_2 (orange spots), a large mismatch would also be evident if these phases were observed together. The spots corresponding to the observed 3R PbI_2 (blue spots), however, shows a perfect overlap with those of cubic $FAPbI_3$. This is identical to the overlap in the Fourier transform in Figure 1b, obtained partly from the perovskite lattice and from the PbI_2 inclusion. Comparing the FT in Figure S3f (Supporting Information) and the simulated SAED pattern in Figure S3g (Supporting Information) clearly illustrates the presence of both the trigonal 3R and the hexagonal 2H phase after extended irradiation. It is thus, clear that $FAPbI_3$ does not degrade directly into hexagonal 2H PbI_2 under electron irradiation, but that trigonal 3R PbI_2 is an intermediate phase. This could explain the common misidentification of degraded $FAPbI_3$ since the plane spacings and square geometry do not immediately change to those of hexagonal 2H PbI_2.

X-ray diffraction (XRD) is often used to determine the presence of PbI_2 in a perovskite film, but this technique alone may not be able to reveal the presence of the trigonal 3R polytype of PbI_2 that we observe in $FAPbI_3$. We simulated XRD patterns based for the cubic $FAPbI_3$, the hexagonal 2H PbI_2 and the trigonal 3R PbI_2 phases, as shown in **Figure 4**. The 2H polytype shows characteristic diffraction peaks that do not overlap with those of either

$FAPbI_3$ or $MAPbI_3$, allowing XRD to detect the presence of this particular polytype in a perovskite film. These peaks are found at 2θ-angles of around 12.7°, 25.9°, and 34.3° ({001}, {$1\bar{1}1$}, and {$\bar{1}12$} planes, respectively) when Cu-Kα X-rays with a wavelength of 1.541 Å are assumed, as seen in Figure 4, with closeups of 11°–14° and 15° —-29° seen in Figures S4 and S5 (Supporting Information), respectively.

However, the observed 3R polytype has a peak at 12.0° ({003} planes corresponding to the interlayer spacing) and at 28.0° ({$\bar{1}14$} planes) that overlaps perfectly with the cubic perovskite 200 reflection. The 12.0° peak is not commonly observed in published XRD data, but this could be due to the strong preferential orientation, with the cubic {100} planes parallel to the substrate found in most perovskite films.[12] As can be seen in Figure 3, the {003} planes are highly inclined relative to the cubic {100} planes and so the Bragg condition for these planes is unlikely to be satisfied in most XRD experiments.

In a thin film consisting purely of $FAPbI_3$, the intensity of the {200} peak should be around 83 % of that of the {100} peak, but these peaks are sometimes found to be almost equal in intensity or even show a reverse intensity relationship, particularly after ageing.[36] This observation indicates a contribution by a phase that does not diffract at 13.9° but does diffract at 28.0°, such as the polytypes we propose. Cordero et al. studied the changes in compressed cubic $FAPbI_3$ powder over time in a humid atmosphere and found a sharp increase in the intensity of the 28.0° {200} peak relative to the 13.9° {100} peak after 100 days, consistent with the formation of the observed PbI_2 at the expense of cubic $FAPbI_3$. Interestingly, they found only a very small signal from 2H PbI_2 at 12.7° and a slightly larger peak around 12.0°,[36] which we believe indicates that most of the PbI_2 had formed in a trigonal polytype. As such, there is evidence for the presence of multiple polytypes of PbI_2 existing within perovskite thin films. Because of the peak overlaps between the 3R PbI_2 and the $FAPbI_3$, it is clear that relying solely on XRD to determine the PbI_2 content of a film is not reliable or advisable, especially if the PbI_2 is present at a low concentration.

To explore the impact on the electronic structure near domains of 3R PbI_2 interfacing coherently with $FAPbI_3$, we performed density functional theory calculations for an interface between the observed PbI_2 polytype and the slightly tetragonally distorted β-$FAPbI_3$ phase. This phase was used to limit the rotational disorder often associated with simulations of interface defects with the cubic phase (see **Figure 5**a and Methods for details). All ions near the interface retain bulk-like coordination and the interface introduces no strong dipole. As seen in Figure 5b using the PBESol approximation for exchange-correlation we found the bandgap of the PbI_2 (2.20 eV) to be higher than that of $FAPbI_3$ (1.27 eV), and we found no states present within the bandgap when near the interface. The calculated valence and conduction band offsets between PbI_2 and $FAPbI_3$ are 0.23 and 0.70 eV, respectively. Qualitatively similar results are obtained at the more accurate HSE+D3+SOC level of theory (see methods) where bandgaps of 1.06 eV (β-$FAPbI_3$) and 2.83 eV (3R-PbI_2) are obtained with valence and conduction band offsets of 0.50 and 1.27 eV, respectively. This confirms that the presence of highly coherently interfaced PbI_2 domains do not induce any trap states that could decrease photovoltaic performance or charge transport properties. These findings therefore give a clear rationale for film growth under slight PbI_2 excess conditions, leading to enhanced performance of photovoltaic devices.[14–17,19–21,24] While such PbI_2 growth appears not to introduce electronically adverse effects, it may also ensure the absence of phases of the second, organohalide precursor (e.g., FAI) that may potentially be detrimental.

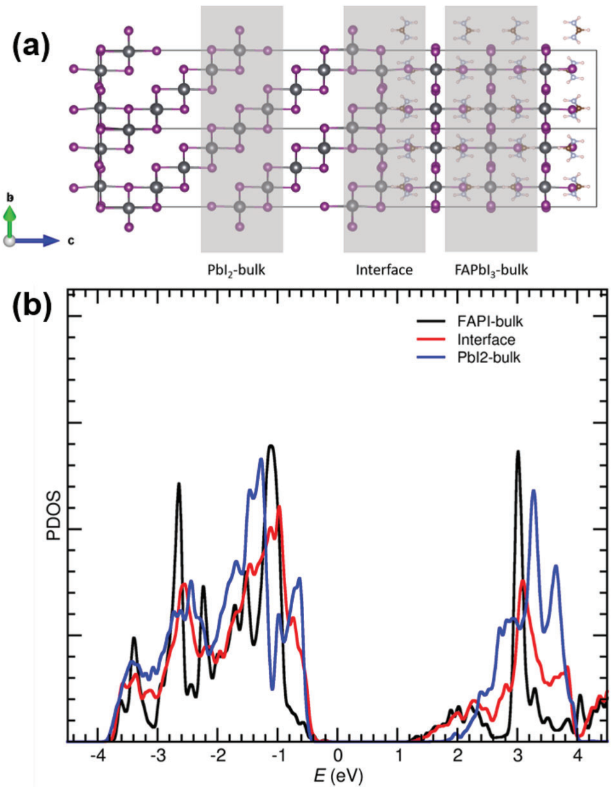

Figure 5. a) Crystal model of the interface used for the density of states calculations with the observed PbI_2 on the left and β-$FAPbI_3$ on the right. The shaded areas indicate regions of bulk-like PbI_2 and $FAPbI_3$ and a region near the interface. b) Projected density of states in the bulk-like and interface regions highlighted in (a). No additional states are introduced by the coherent interface.

3. Conclusion

In summary, we have shown the presence of coherently interfacing domains of PbI_2 within the cubic $FAPbI_3$ lattice comprising a 3R trigonal polytype of PbI_2. The trigonal polytype contains many plane spacings similar to those found in cubic $FAPbI_3$, making it difficult to detect this polytype using XRD alone. The high degree of coherency does not introduce any significant number of structural defects at the interface between the two materials. As such, the coherent interface does not introduce any new electronic states in the bandgap of the materials or at the interface itself, making it electronically benign. Overall, our findings explain how the inclusion of a small amount of 3R PbI_2 in perovskite light-absorption layers can help improve the overall solar cell performance by acting as a coherent seed for perovskite growth without introducing interfacial defects. It is likely that the generally flexible nature of PbI_2 is what enables PbI_2 to passivate defects in general, and it is clear that a better understanding of the influence of PbI_2's polytypism on perovskite solar cells is necessary.

4. Experimental Section

Sample Preparation: $FAPbI_3$ thin films were deposited on the carbon-coated side of 300-mesh copper TEM grids. Immediately prior to deposition, the grids were O_2-plasma cleaned for 0.3 min.

$CH(NH)_2I$ (FAI) and PbI_2 were co-evaporated in a customised thermal evaporation chamber described previously.[37] Heating of the sources started once the chamber pressure fell below 5×10^{-6} mbar. The PbI_2 rate was kept constant at 0.23 Ås^{-1}, measured using a gold-plated quartz microbalance (QMB). This FAI crucible temperature was kept around 150 °C during deposition. During deposition, the pressure increased to 1-2 $\times 10^{-5}$ mbar. The duration of the overall perovskite deposition was controlled such that the film thickness was 90 nm. After deposition, the films were annealed at 170 °C for 1 min. The films were stored in a nitrogen-filled glove box after preparation and transported to the microscope in a triple-sealed nitrogen atmosphere to prevent exposure to moisture. All samples were loaded rapidly into the microscope, being in contact with air for less than a minute.

Perovskite film thicknesses were determined from calibration of material deposition rates of the two sources according to quartz microbalance readings inside the vacuum chamber, supported by film depositions on hard transparent quartz substrates for which film thickness readings were determined from a combination of Dektak profilometer readings and optical transmission measurements.

Image Acquisition: Microscopy was performed on a JEOL ARM-200F cold FEG, Cs probe corrected STEM at 200 kV acceleration voltage, 23–24 mrad convergence angle, using an annular dark field detector at 8 cm camera length, resulting in inner and outer collection angles of 33 and 120.77 mrad, respectively for LAADF imaging. Both room temperature and cryogenic conditions were used, and the cryogenic conditions did not noticeably reduce the beam sensitivity of the $FAPbI_3$ thin films, so all imaging was done at room temperature. Similarly, no noticeable difference in beam sensitivity was found between 200 and 300 kV acceleration voltage. All imaging presented in the manuscript was at 200 kV. All alignments and focusing were done away from the areas imaged to reduce electron beam-induced damage to the material. All micrographs were obtained without tilting the sample to reduce the beam damage.

Diffraction Simulation: Simulations of the SAED and XRD patterns were performed using commercial CrystalDiffract and SingleCrystal software and were based on 2H PbI_2 (ICSD number 68819), cubic $FAPbI_3$ (found at https://github.com/WMD-group/hybrid-perovskites/blob/fe4b188d5c7549050d9994c64bc86636968addd6/2014_cubic_halides_PBEsol/FAPbI3.cif), and 3R PbI_2 (available for download with this paper).

Theoretical Calculations: First principles density functional theory calculations were performed using the projector augmented wave method, which was implemented in the Vienna Ab initio Simulation Package (VASP).[38,39] Calculations for the bulk $FAPbI_3$ and PbI_2 phases were carried with two different approximations for the exchange-correlation functional: the generalized gradient approximation functional PBESol and the hybrid functional HSE06[40] (with 40% Hartree-Fock exchange and spin-orbit coupling included along with the D3 Grimme dispersion correction to describe the Van der Waals interactions,[41] hereafter HSE+D3+SOC). It considered β-$FAPbI_3$ rather than the room temperature cubic $FAPbI_3$ phase for constructing the interfaces models. β-$FAPbI_3$ was predicted to be stable below room temperature and was slightly tetragonally distorted structure.[42] This had the advantage that the FA molecules orient in preferred directions preventing issues associated with rotational disorder one often found in simulations of interface defects with the cubic phase. The bulk β-$FAPbI_3$ unit cell was optimized at the PBESol level using a $6 \times 6 \times 4$ gamma centered k-point grid for Brillouin zone sampling and a 500 eV plane wave cut-off until all forces were less than 0.01 eVÅ^{-1} yielding lattice constants $a = 9.00$ and $c = 12.51$ Å and a bandgap $E_g = 1.27$ eV. This corresponds to a pseudocubic structure with $a = 6.36$ and $c = 6.23$ Å, very close to the experimental lattice constant for the room temperature phase ($c = 6.36$ Å). The trigonal PbI_2 until cell was optimized using the same plane wave cut-off and a $6 \times 6 \times 6$ k-point grid yielding $a = 7.60$ Å, $\alpha = 34.80°$, and $E_g = 2.20$ eV. A coherent interface between β-$FAPbI_3$ and PbI_2 could be produced by applying less than 1% strain (which it apply to PbI_2 as the secondary phase). The interface joins the β-$FAPbI_3$ (001) surface to the PbI_2 (104) surface with β-$FAPbI_3$[110] parallel to PbI_2[010]. A supercell containing ≈ 25 Å thick grains of β-$FAPbI_3$ and PbI_2 with two equivalent periodically repeated interfaces and optimized using a $4 \times 4 \times 1$ k-point grid (including optimization of the cell vector perpendicular to the interfaces). The electronic density of states (DOS) projected on various regions within the supercell was then calculated to investigate whether any states were present within the β-$FAPbI_3$ bandgap. The projected DOS indicated the PbI_2 and interface bands lie above and below the conduction and valence bands of β-$FAPbI_3$, respectively and the absence of any gap states. This analysis also suggests the conduction band offset between the two materials was larger than the valence band offset. Structures were visualized using the VESTA package.[43]

To provide a more precise determination of the band offsets we also compute the plane averaged electrostatic potential for the supercell and align this to corresponding calculations for the separate β-$FAPbI_3$ and PbI_2 bulk phases at both the PBESol and HSE+D3+SOC levels of theory.[44,45] Using HSE+D3+SOC with structures optimized at the PBESol level of theory yields bulk bandgaps of 1.07 eV (β-$FAPbI_3$) and 2.89 eV (PbI_2). The calculated valence band offsets are 0.23 eV (PBESol) and 0.50 eV (HSE+D3+SOC) and the conduction band offsets are 0.70 eV (PBESol) and 1.27 eV (HSE+D3+SOC).

Supporting Information

Supporting Information is available from the Wiley Online Library or from the author.

Acknowledgements

The authors gratefully acknowledge financial support from the Engineering and Physical Sciences Research Council (UK) (EPSRC) through grant numbers EP/P033229/1 and EP/V010840/1, and through the EPSRC CDT for New and Sustainable Photovoltaics. L.M.H. acknowledges support through a Hans Fischer Senior Fellowship from the Technical University of Munich's Institute for Advanced Study, funded by the German Excellence Initiative. M.B.J. acknowledges support from the EPSRC UK through the award of an Established Career Fellowship (EP/T025077/1). The authors thank the David Cockayne Centre for Electron Microscopy, University of Oxford, for access and support in the use of the JEOL ARM200F instrument (proposal number EP/K040375/1). L.M.H and M.B.J. thank the Humboldt Foundation for Research Awards. K.M. acknowledges support from EPSRC (EP/P023843/1). Via our membership of the UK's HEC Materials Chemistry Consortium, which is funded by EPSRC (EP/R029431), this work used the ARCHER2 UK National Supercomputing Service (http://www.archer2.ac.uk). This work also made use of the Viking Cluster, which was a high-performance computer facility provided by the University of York.

Conflict of Interest

The authors declare no conflict of interest.

Author Contributions

M.U.R. designed and carried out the electron microscope studies, and analyzed and interpreted data. J.B and K.B.L. prepared the samples. K.M. performed the density functional theory calculations. M.B.J., P.D.N., and L.M.H. designed the study, interpreted data, and supervised M.U.R. M.U.R wrote the manuscript with input from all co-authors.

Data Availability Statement

The data that support the findings of this study are available from the corresponding author upon reasonable request.

Keywords

electron microscopy, electronic structure of crystallographic interfaces, lead iodide polytypes, perovskite solar cells

Received: March 24, 2023
Revised: May 25, 2023
Published online: July 14, 2023

[1] NREL, Best research-cell efficiency chart, https://www.nrel.gov/pv/cell-efficiency.html, **2023**, Accessed: 2023-06-12.
[2] L. M. Herz, *ACS Energy Lett.* **2017**, *2*, 1539.
[3] C. Wehrenfennig, G. E. Eperon, M. B. Johnston, H. J. Snaith, L. M. Herz, *Adv. Mater.* **2014**, *26*, 1584.
[4] M. M. Lee, J. Teuscher, T. Miyasaka, T. N. Murakami, H. J. Snaith, *Science* **2012**, *338*, 643.
[5] H.-S. Kim, C.-R. Lee, J.-H. Im, K.-B. Lee, T. Moehl, A. Marchioro, S.-J. Moon, R. Humphry-Baker, J.-H. Yum, J. E. Moser, et al., *Sci. Rep.* **2012**, *2*, 1.
[6] M. Liu, M. B. Johnston, H. J. Snaith, *Nature* **2013**, *501*, 395.
[7] K. B. Lohmann, S. G. Motti, R. D. Oliver, A. J. Ramadan, H. C. Sansom, Q. Yuan, K. A. Elmestekawy, J. B. Patel, J. M. Ball, L. M. Herz, H. J. Snaith, M. B. Johnston, *ACS Energy Lett.* **2022**, *7*, 1903.
[8] S. D. Stranks, V. M. Burlakov, T. Leijtens, J. M. Ball, A. Goriely, H. J. Snaith, *Phys. Rev. Appl.* **2014**, *2*, 034007.
[9] M. J. Trimpl, A. D. Wright, K. Schutt, L. R. Buizza, Z. Wang, M. B. Johnston, H. J. Snaith, P. Müller-Buschbaum, L. M. Herz, *Adv. Funct. Mater.* **2020**, *30*, 2004312.
[10] W.-J. Yin, T. Shi, Y. Yan, *Appl. Phys. Lett.* **2014**, *104*, 063903.
[11] J. M. Ball, A. Petrozza, *Nat. Energy* **2016**, *1*, 1.
[12] M. U. Rothmann, J. S. Kim, J. Borchert, K. B. Lohmann, C. M. O'Leary, A. A. Sheader, L. Clark, H. J. Snaith, M. B. Johnston, P. D. Nellist, L. M. Herz, *Science* **2020**, *370*, eabb5940.
[13] X. Yang, D. Luo, Y. Xiang, L. Zhao, M. Anaya, Y. Shen, J. Wu, W. Yang, Y.-H. Chiang, Y. Tu, R. Su, Q. Hu, H. Yu, G. Shao, W. Huang, T. P. Russell, Q. Gong, S. D. Stranks, W. Zhang, R. Zhu, *Adv. Mater.* **2021**, *33*, 2006435.
[14] Q. Chen, H. Zhou, T.-B. Song, S. Luo, Z. Hong, H.-S. Duan, L. Dou, Y. Liu, Y. Yang, *Nano Lett.* **2014**, *14*, 4158.
[15] L. Wang, C. McCleese, A. Kovalsky, Y. Zhao, C. Burda, *J. Am. Chem. Soc.* **2014**, *136*, 12205.
[16] D. H. Cao, C. C. Stoumpos, C. D. Malliakas, M. J. Katz, O. K. Farha, J. T. Hupp, M. G. Kanatzidis, *APL Mater.* **2014**, *2*, 091101.
[17] Y. C. Kim, N. J. Jeon, J. H. Noh, W. S. Yang, J. Seo, J. S. Yun, A. Ho-Baillie, S. Huang, M. A. Green, J. Seidel, T. K. Ahn, S. I. Seok, *Adv. Energy Mater.* **2016**, *6*, 1502104.
[18] Y. C. Kim, N. J. Jeon, J. H. Noh, W. S. Yang, J. Seo, J. S. Yun, A. Ho-Baillie, S. Huang, M. A. Green, J. Seidel, T. K. Ahn, S. I. Seok, *Adv. Energy Mater.* **2016**, *6*, 1502104.
[19] V. Kapoor, A. Bashir, L. J. Haur, A. Bruno, S. Shukla, A. Priyadarshi, N. Mathews, S. Mhaisalkar, *Energy Technol.* **2017**, *5*, 1880.
[20] Y. Chen, Q. Meng, Y. Xiao, X. Zhang, J. Sun, C. B. Han, H. Gao, Y. Zhang, Y. Lu, H. Yan, *ACS Appl. Mater. Interfaces* **2019**, *11*, 44101.
[21] B. Shi, X. Yao, F. Hou, S. Guo, Y. Li, C. Wei, Y. Ding, Y. Li, Y. Zhao, X. Zhang, *J. Phys. Chem. C* **2018**, *122*, 21269.
[22] J. B. Patel, Q. Lin, O. Zadvorna, C. L. Davies, L. M. Herz, M. B. Johnston, *J. Phys. Chem. Lett.* **2018**, *9*, 263.
[23] K. B. Lohmann, J. B. Patel, M. U. Rothmann, C. Q. Xia, R. D. Oliver, L. M. Herz, H. J. Snaith, M. B. Johnston, *ACS Energy Lett.* **2020**, *5*, 710.
[24] Y. H. Lee, J. Luo, R. Humphry-Baker, P. Gao, M. Grätzel, M. K. Nazeeruddin, *Adv. Funct. Mater.* **2015**, *25*, 3925.
[25] F. Liu, Q. Dong, M. K. Wong, A. B. Djurišić, A. Ng, Z. Ren, Q. Shen, C. Surya, W. K. Chan, J. Wang, A. M. C. Ng, C. Liao, H. Li, K. Shih, C. Wei, H. Su, J. Dai, *Adv. Energy Mater.* **2016**, *6*, 1502206.
[26] J. an Yang, A. Xiao, L. Xie, K. Liao, X. Deng, C. Li, A. Wang, Y. Xiang, T. Li, F. Hao, *Electrochim. Acta* **2020**, *338*, 135697.
[27] B.-w. Park, N. Kedem, M. Kulbak, W. S. Yang, N. J. Jeon, J. Seo, G. Kim, K. J. Kim, T. J. Shin, G. Hodes, D. Cahen, S. I. Seok, *Nat. Commun.* **2018**, *9*, 1.
[28] B. Roose, K. Dey, Y.-H. Chiang, R. H. Friend, S. D. Stranks, *J. Phys. Chem. Lett.* **2020**, *11*, 6505.
[29] H. J. Jung, C. C. Stompus, M. G. Kanatzidis, V. P. Dravid, *Nano Lett.* **2019**, *19*, 6109.
[30] M. Chand, G. Trigunayat, *Acta Cryst.* **1975**, *31*, 1222.
[31] T. Minagawa, *J. Appl. Crystallogr.* **1979**, *12*, 57.
[32] P. A. Beckmann, *Cryst. Res. Technol.* **2010**, *45*, 455.
[33] M. U. Rothmann, W. Li, Y. Zhu, U. Bach, L. Spiccia, J. Etheridge, Y.-B. Cheng, *Nat. Commun.* **2017**, *8*, 1.
[34] M. U. Rothmann, W. Li, Y. Zhu, A. Liu, Z. Ku, U. Bach, J. Etheridge, Y.-B. Cheng, *Adv. Mater.* **2018**, *30*, 1800629.
[35] C.-Y. Chang, Y.-C. Huang, C.-S. Tsao, W.-F. Su, *ACS Appl. Mater. Interfaces* **2016**, *8*, 26712.
[36] F. Cordero, F. Craciun, F. Trequattrini, A. Generosi, B. Paci, A. M. Paoletti, G. Pennesi, *J. Phys. Chem. Lett.* **2019**, *10*, 2463.
[37] J. Borchert, R. L. Milot, J. B. Patel, C. L. Davies, A. D. Wright, L. Martinez Maestro, H. J. Snaith, L. M. Herz, M. B. Johnston, *ACS Energy Lett.* **2017**, *2*, 2799.
[38] G. Kresse, J. Furthmüller, *Comput. Mater. Sci.* **1996**, *6*, 15.
[39] G. Kresse, J. Furthmüller, *Phys. Rev. B* **1996**, *54*, 11169.
[40] A. V. Krukau, G. E. Scuseria, J. P. Perdew, A. Savin, *J. Chem. Phys.* **2008**, *129*, 124103.
[41] S. Grimme, *J. Comput. Chem.* **2004**, *25*, 1463.
[42] O. J. Weber, D. Ghosh, S. Gaines, P. F. Henry, A. B. Walker, M. S. Islam, M. T. Weller, *Chem. Mater.* **2018**, *30*, 11.
[43] K. Momma, F. Izumi, *J. Appl. Crystallogr.* **2011**, *44*, 1272.
[44] Y.-H. Li, A. Walsh, S. Chen, W.-J. Yin, J.-H. Yang, J. Li, J. L. F. Da Silva, X. G. Gong, S.-H. Wei, *Appl. Phys. Lett.* **2009**, *94*, 212109.
[45] A. C. M. Padilha, K. P. McKenna, *Phys. Rev. Mater.* **2018**, *2*, 045001.